Article

Two-Bubble Acoustic Tweezing Cytometry for Biomechanical Probing and Stimulation of Cells

Di Chen,[1] Yubing Sun,[2] Madhu S. R. Gudur,[1] Yi-Sing Hsiao,[1] Ziqi Wu,[1] Jianping Fu,[1,2,*] and Cheri X. Deng[1,*]
[1]Department of Biomedical Engineering and [2]Department of Mechanical Engineering, University of Michigan, Ann Arbor, Michigan

ABSTRACT The study of mechanotransduction relies on tools that are capable of applying mechanical forces to elicit and assess cellular responses. Here we report a new (to our knowledge) technique, called two-bubble acoustic tweezing cytometry (TB-ATC), for generating spatiotemporally controlled subcellular mechanical forces on live cells by acoustic actuation of paired microbubbles targeted to the cell adhesion receptor integrin. By measuring the ultrasound-induced activities of cell-bound microbubbles and the actin cytoskeleton contractile force responses, we determine that TB-ATC elicits mechanoresponsive cellular changes *via* cyclic, paired displacements of integrin-bound microbubbles driven by the attractive secondary acoustic radiation force (sARF) between the bubbles in an ultrasound field. We demonstrate the feasibility of dual-mode TB-ATC for both subcellular probing and mechanical stimulation. By exploiting the robust and unique interaction of ultrasound with microbubbles, TB-ATC provides distinct advantages for experimentation and quantification of applied forces and cellular responses for biomechanical probing and stimulation of cells.

INTRODUCTION

Cellular mechanosensitivity to extracellular mechanical signals is central to many developmental, physiological, and pathological processes and affects many cell functions, including growth, migration, differentiation, and apoptosis (1–3). Mechanotransduction involves the transmission of extracellular forces through adhesion receptors and actin cytoskeleton (CSK) followed by the conversion of these signals into intracellular biochemical events (4–7). Bioengineering tools that can apply controlled forces to elicit and assess cellular responses are essential for investigating the molecular mechanisms involved in mechanoresponsive cellular behaviors. Successful translation of insights and discoveries obtained from mechanotransduction studies also critically depends on the availability and convenient implementation of such tools.

Single-cell techniques such as micropipette aspiration (8), optical tweezers (9), and atomic force microscopy (AFM) (10) are used to apply localized forces to single cells and quantify cellular mechanical properties, but generally are not compatible with established biochemical assays involving an ensemble of cells. Magnetic twisting cytometry (MTC) generates twisting stress on multiple cells simultaneously using functionalized magnetic microbeads attached to cells (11–13). However, the solid microbeads used in optical tweezers and MTC can elicit cell internalization, are difficult to remove from the cells, and may interfere with downstream studies or translational applications using the treated cells.

We recently developed a new technique, to our knowledge, called acoustic tweezing cytometry (ATC) (14), that can induce robust reactive cellular contractile force changes by acoustically actuating microbubbles targeted to integrin receptors (Fig. 1, *a* and *c*). Microbubbles encapsulated by a thin (e.g., ~5 nm) shell of lipid or protein molecules (e.g., albumin) have been used as ultrasound imaging contrast agents in echocardiography (15,16). They are highly responsive to ultrasound owing to large differences in the acoustic properties of the surrounding liquid and the gas core (17,18), and exhibit a variety of behaviors, such as cavitation (bubble expansion/contraction or collapse) (17,18). Cavitation generates shear stress and/or a mechanical impact on nearby cells or objects (17,19–21) via fluid streaming and fast fluid jets (22), and has been exploited to disrupt the cell membrane and thus facilitate nonviral gene delivery (22,23). A microbubble is also subjected to the primary acoustic radiation force (pARF) or the primary Bjerknes force, a net force in the direction of acoustic wave propagation due to acoustic momentum transfer (24,25).

Interestingly, interactions among bubbles in an ultrasound field occur due to multiple scattering of the ultrasound field, resulting in microbubble dynamic behaviors that are distinctively different from those of single microbubbles (26). With multiple scattering, a microbubble is influenced by not only the incident or primary ultrasound field but also the scattering of the ultrasound fields of the primary field by other bubbles. The scattered fields generate the secondary acoustic radiation force (sARF) or the secondary Bjerknes force (24) on neighboring bubbles, which can dramatically affect microbubble behaviors. Notably, the sARFs between two bubbles pulsating in phase in an ultrasound field are

Submitted June 25, 2014, and accepted for publication November 4, 2014.
*Correspondence: cxdeng@umich.edu or jpfu@umich.edu
Editor: Christopher Yip.

0006-3495/15/01/0032/11 $2.00
http://dx.doi.org/10.1016/j.bpj.2014.11.050

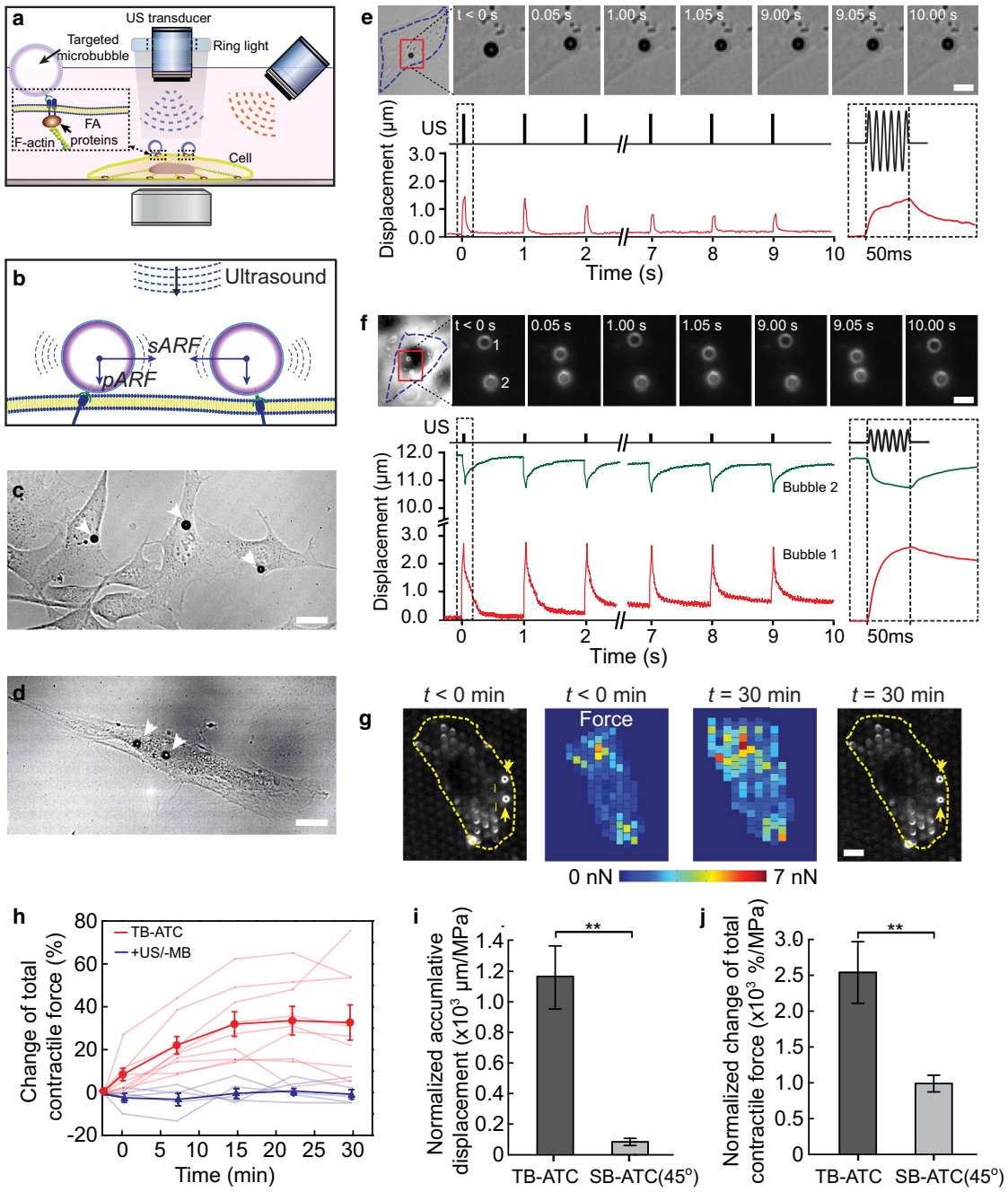

FIGURE 1 Single-bubble (SB) and two-bubble (TB) acoustic tweezing cytometry (ATC). (*a*) Experimental setup of ATC using oblique or vertical ultrasound application. (*b*) Schematics of pARF and the attractive sARF exerted on two microbubbles. (*c* and *d*) Brightfield images showing one (*c*) or two (*d*) microbubbles attached to single cells (NIH 3T3 fibroblasts in *c*; hMSCs in *d*). (*e*) Brightfield images and line plot showing the temporal evolution of the lateral displacement of a single bubble attached to an NIH 3T3 fibroblast subjected to ATC. The incident angle of the ultrasound is 45° with respect to the vertical direction. (*f*) Brightfield images and line plot of lateral displacements of a pair of microbubbles subjected to TB-ATC. The incident angle of the ultrasound is 0° with respect to the vertical direction. Insets in *e* and *f*: bubble displacements during the first ultrasound pulse. (*g*) Pseudo-color images showing the contractile force of single NIH 3T3 fibroblasts measured by the micropost technique before and 30 min after TB-ATC application. The TB-ATC application lasted 10 s from $t = 0$ min. Yellow arrows point to integrin-bound microbubbles. (*h*) Change of total CSK contractile force for single cells (relative to contractility before ultrasound) with bubbles ($n = 9$) and without microbubbles (+US/−MB, $n = 5$) subjected to 10 s TB-ATC application. (*i* and *j*) Accumulative displacements of bubbles and contractile force changes divided by the acoustic pressure. Ultrasound parameters: frequency 1.25 MHz, acoustic pressure 0.05 MPa (SB-ATC) or 0.015 MPa (TB-ATC), pulse duration 50 ms, and PRF 1 Hz. Error bars, mean ± SE. $^{**}p < 0.01$, Student's *t*-test. To see this figure in color, go online.

attractive and point directly toward each other regardless of the primary wave direction (Fig. 1 *b*). Its magnitude is inversely proportional to the square of the distance between the bubbles, resembling the gravitational force between two masses or the electrostatic force between two charges in classic field theories.

Here we report a novel (to our knowledge) technique, called two-bubble (TB)-ATC, that exploits the sARF to apply spatiotemporally controlled mechanical forces to live cells by displacing paired microbubbles anchored at two subcellular locations (Fig. 1, *a*, *b*, and *d*). The unique mechanism of force application provides experimentation and quantification advantages for both probing of subcellular properties and biomechanical stimulations in an integrated platform.

MATERIALS AND METHODS

Cell culture

NIH 3T3 mouse fibroblasts (ATCC) and early passages (2–4) of human mesenchymal stem cells (hMSCs) (Lonza) were used. NIH 3T3 cells were maintained at 37°C and 5% CO_2 in growth medium consisting of low-glucose Dulbecco's modified Eagle's medium (Invitrogen) supplemented with 10% bovine serum (Invitrogen), 1% L-glutamine, and 1% penicillin/streptomycin. The hMSCs were maintained in MSC growth medium (Lonza) at 37°C and 5% CO_2, and the culture medium was replaced every 2 days. Cells were harvested 8 h before experiments and plated in fibronectin-coated polydimethylsiloxane (PDMS) micropost arrays or 35 mm glass-bottom dishes (3000 cells cm^{-2}).

Targeted microbubbles and attachment to cells

Targesphere-SA microbubbles (Targeson) with a mean diameter of 1.8 ± 0.2 μm ($n = 208$) were mixed with biotinylated Arg-Gly-Asp (RGD) peptides (Peptides International) for 20 min at room temperature, at a volume ratio of 5:1 for Targesphere-SA microbubbles (5×10^8 mL^{-1}) and RGD (0.01 mg mL^{-1}) to form RGD-coated microbubbles. AcLDL-coated microbubbles were formed by mixing Targesphere-SA microbubbles with acetylated low-density lipoprotein (AcLDL; Invitrogen) for 24 h at 4°C at a volume ratio of 5:1 for microbubbles (5×10^8 mL^{-1}) and AcLDL (2.5 mg mL^{-1}). To conjugate RGD- or AcLDL-coated microbubbles with cells, the culture medium was removed, followed by immediate addition of 20 μL of the functionalized microbubbles. The cell culture dish was then flipped upside down for 10 min to permit bubble attachment to cells via RGD-integrin binding or nonspecific receptor binding (for AcLDL-coated microbubbles). The dish was flipped back and unbound bubbles were removed by gentle washing with culture medium. The concentration of microbubbles was selected to ensure that only one or two bubbles were attached to each single cell.

Ultrasound system and generation of ultrasound pulses

A 1.25 MHz planar circular transducer (Advanced Devices; 3 dB beam width of 2 mm at a Rayleigh distance of 7.5 mm) or a 10 MHz focused transducer (Olympus; 3 dB beam width of 1.6 mm at a Rayleigh distance of 11.25 mm), driven by a waveform generator (Agilent Technologies 33250A) and a 75 W power amplifier (Amplifier Research 75A250), was used to generate ultrasound pulses with the desired parameters, including acoustic pressure, pulse duration, and pulse repetition frequency (PRF). The transducer, with its active surface submerged in the culture medium, was positioned either vertically (0°) facing downward or at an angle of 45° to the downward vertical direction (Fig. 1 *a*), at the Rayleigh distance from the adherent cells at the bottom of the dish. The transducer was characterized in free field using a 40 μm needle hydrophone (HPM04/1; Precision Acoustics).

To minimize artifacts associated with ultrasound standing waves in the cell culture dish, we implemented a chirping exposure strategy to decrease the constructive interference of incoming and reflected ultrasound waves (27). Chirp pulses (pulse duration 50 ms pulse) were produced by sweeping the driving frequency linearly around the center frequency of 1.25 MHz from 1.1 to 1.4 MHz. The acoustic pressure amplitude for the pulses was maintained nearly constant, within 5% of 0.05 MPa for SB-ATC and 0.015 MPa for TB-ATC, by modulating the amplitude of the driving signals to compensate for the transducer frequency response.

As the wavelength of ultrasound is 1.5–0.15 mm corresponding to an ultrasound frequency of 1–10 MHz, pressure doubling due to reflections from the dish bottom was accounted for by the cells/microbubbles (~10 μm height from the dish bottom) in our studies.

Monitoring and characterization of ultrasound-driven microbubble kinetics using high-speed videomicroscopy

An inverted microscope (Eclipse Ti-U; Nikon) was used for observation of cells and microbubble activities during ultrasound application. Operation of a high-speed camera (Photron FASTCAM SA1) was synchronized with the application of ultrasound pulses to capture the dynamic microbubble activities driven by ultrasound at a frame rate of 5000 frames s^{-1}. We used pixel intensity and its spatial gradient in the acquired images to track microbubbles by employing a customized algorithm refined from built-in circle-tracking algorithms in MATLAB (MathWorks). The position and radius of a microbubble were estimated with a subpixel resolution of 50 nm. The displacement of a microbubble was obtained from these images as a function of time before, during, and after ultrasound application. The accumulative bubble displacement was estimated as the sum of the bubble displacements sustained during ultrasound application.

Theoretical calculation of streaming velocity, pARF, and sARF

The peak streaming velocity u_0 near the bubble surface is approximated as $u_0 = 2\pi f \varepsilon^2 R_0$ (21,28), where R_0 is the stable bubble radius before ultrasound application and f is the ultrasound frequency. $\varepsilon = \Delta R/R_0$, where $\Delta R = R(t) - R_0$, and $R(t)$ can be calculated numerically by solving the Rayleigh, Plesset, Noltingk, Neppiras, and Poritsky (RPNNP) equation (19), the general equation for bubble oscillation driven by ultrasound:

$$\ddot{R}R\rho + \frac{3}{2}\rho\dot{R}^2 = \left(P_0 + \frac{2\sigma}{R_0}\right)\left(\frac{R_0}{R}\right)^{3\gamma} - P_0 - \frac{2\sigma}{R} - 2S_p\left(\frac{1}{R_0} - \frac{1}{R}\right) - \left(\frac{4\mu}{R^2} + \frac{S_f}{4\pi R^3}\right)\dot{R}R + P_{ac},$$

where $R(t)$ is the instantaneous bubble radius as a function of time t; P_0 is the ambient pressure; ρ, σ, and μ are the density, surface tension, and viscosity of the surrounding medium, respectively; γ is the polytropic exponent of the bubble; and S_p and S_f are the bubble shell elasticity (stiffness) and viscosity (friction), respectively. $P_{ac} = P_A \cos(2\pi f t)$ is the applied acoustic pressure, with P_A and f as the peak pressure and frequency, respectively, of the ultrasound field. A first-order assumption was made regarding the frequency dependence of the properties of the microbubbles and the surrounding medium.

The pARF was calculated as described previously (24) using

$$F_P = \frac{2\pi P_A^2 D R_0}{\rho c \omega T} \frac{2\beta_{tot}/\omega}{\left[(\omega_0/\omega)^2 - 1\right]^2 + (2\beta_{tot}/\omega)^2},$$

where c is the speed of sound in medium, D is the duration of each pulse, and T is the pulse repetition period. To calculate the force during each ultrasound pulse, we allowed $D / T = 1$. We estimated the parameters in the above equation using previously reported parameters (29). The dimensionless damping coefficient $\beta_{tot} = \delta_{tot}\,\omega_0/2$, where δ_{tot} is the total damping constant computed using $\delta_{tot} = \omega R_0/c + 4\mu/\omega\rho R_0^2 + S_f/4\pi\rho R_0^3\omega$; $\omega = 2\pi f$, where f is the center frequency of applied ultrasound; and $\omega_0 = 2\pi f_0$, where f_0 is the resonant frequency of microbubble that is computed using $f_0 = 1/2\pi \cdot (3\gamma P_0/\rho R_0^2 + 2S_p/\rho R_0^3)^{1/2}$, where γ is the polytropic exponent of the bubble. A polytropic process occurs between the isothermal process and the adiabatic process in practice, which bears the expression of $PV^\gamma =$ constant, with γ as the polytropic exponent.

The sARF F_s was calculated according to a previously reported expression (24) as

$$F_s = -\frac{2\pi\rho}{9}(\omega P_A)^2 \kappa_1^2 \frac{R_1^3 R_2^3}{d^2},$$

where κ_1 is the compressibility of bubble 1; R_1 and R_2 are the radii of bubbles 1 and 2, respectively; and d is the separation distance between the bubbles. In all plots, F_s is presented by its absolute value.

Previous studies have demonstrated the theoretical expressions of acoustic radiation forces in terms of ultrasound parameters such as frequency and acoustic pressure. Therefore, in this study, we calculated the pARF and sARF acting on the microbubbles by using the measured acoustic pressure amplitude of the ultrasound field in our experiments, along with the known ultrasound center frequency, bubble size, and other parameters listed in Table 1.

Measurement of microstreaming and shear stress generated by a cavitating microbubble

Microbubbles expand and contract driven by ultrasound application, and generate microstreaming surrounding the bubble (28). We used micro-particle image velocimetry (μPIV), with 0.5 μm diameter polystyrene particles (Thermo Scientific) as tracers, to measure the flow velocity near a cavitating RGD microbubble attached to a cell, and calculated the resulting shear stress on the cell. First, the tracer particles in a stock solution (1.46×10^{11} particles mL^{-1}) were diluted in deionized water at a 1:2 ratio (v/v). Then, 2 μL of tracer solution was added to the culture medium before ultrasound pulses (1.25 MHz, pulse duration 10 ms, pulse repetition 1 Hz) were applied at different acoustic pressure amplitudes. A region of interest near a cavitating microbubble was recorded continuously with a high-speed camera (Fastcam SA1; Photron) at 20,000 frames/s. We obtained the velocities of the tracer particles and thus the streaming velocity field by tracking the positions of the particles over time from the recorded image sequence using ImageJ (National Institutes of Health). We calculated the shear stress τ exerted on the cell membrane by microstreaming of the medium using $\tau = \mu\Delta u/\Delta y$, where μ is the medium viscosity (7.26×10^{-4}Pa · s), Δu is the flow velocity difference between the bubble equator plane and the cell membrane, and Δy is considered to be the same as the bubble radius.

TABLE 1 Parameters used in the theoretical calculation

Notation		Value used
Bubble properties		
S_f	shell viscosity (friction, kg/s)	0.15×10^{-6} (42)
S_p	shell elasticity (stiffness, N/m)	1.64 (42)
γ	polytropic exponent of gas	1.06 (29)
κ_1	compressibility (m^2/N)	5×10^{-7} (24)
Surrounding medium		
ρ	density (kg/m^3)	998 (43)
σ	surface tension (N/m)	0.072
μ	viscosity (Pa·s)	0.0007 (43)
c	speed of sound (m/s)	1500
Others		
P_0	ambient pressure (Pa)	101×10^3

Quantification of cellular traction forces using PDMS microposts

Fluorescent images of the tops of PDMS microposts underlying adherent cells were obtained and processed using a custom-developed MATLAB program (30) to quantify deflections of PDMS microposts from their unbent, unloaded positions, which were then converted to horizontal traction forces by multiplying with the nominal spring constant of the PDMS microposts.

RESULTS

Displacements of integrin-anchored microbubbles by pARF and sARF

To acoustically actuate or excite cell-bound microbubbles, we employed oblique (e.g., 45° with respect to the downward vertical direction) or vertical (e.g., 0°) application of ultrasound pulses (Fig. 1 *a*), and continuously monitored the kinetics of the microbubbles using high-speed videomicroscopy. In single-bubble (SB)-ATC, where individual microbubbles are excited by ultrasound pulses without mutual interactions among them (Fig. 1 *c*), the application of oblique ultrasound (45°) generates a pARF on single RGD microbubbles bound to cells. The horizontal component of the pARF can induce horizontal or lateral movements of individual microbubbles on the cell surface, whereas the downward component compresses the RGD bubbles against the cell membrane. The application of multiple ultrasound pulses repeatedly displaces the individual cell-bound RGD microbubbles. As shown by the example in Fig. 1 *e* and Movie S1 in the Supporting Material, with ultrasound pulses with a center frequency of 1.25 MHz, acoustic pressure of 0.05 MPa, duration of each pulse of 50 ms, and PRF of 1 Hz, the bubbles retracted back toward their original locations after each ultrasound pulse due to the restoring force in the strained bubble-integrin-CSK linkage.

In contrast, TB-ATC drove a pair of cell-bound RGD microbubbles at separate subcellular locations directly and efficiently toward each other by the attractive sARF (Fig. 1, *d* and *f*; Movie S2), even with low-pressure ultrasound pulses (e.g., 0.015 MPa) and downward ultrasound application, where the pARF contributed minimally to the observed lateral bubble displacements. Interesting, multiple ultrasound pulses (1.25 MHz, 0.015 MPa, pulse duration 50 ms, and PRF 1 Hz) generated paired, cyclic displacements of RGD microbubbles in a correlated fashion (Fig. 1 *f*). Notably, the two RGD microbubbles often

exhibited displacements with different amplitudes (Fig. 1 *f*). As the bubbles were subjected to the sARF of the same magnitude, this displacement difference revealed subcellular mechanical properties and reactive CSK contractile forces at the two subcellular locations.

We assessed the dynamic evolution of cellular actin CSK contractile forces of NIH 3T3 fibroblasts upon TB-ATC application using an array of uniformly spaced, fibronectin-coated PDMS microposts as subcellular live-cell force sensors (31). TB-ATC application for 10 s (0.015 MPa, pulse duration 50 ms, PRF 1 Hz) generated a sustained increase of CSK contractility in NIH 3T3 fibroblasts for more than 30 min (Fig. 1, *g* and *h*), with a global reactive pattern throughout the whole cell in response to the local force of TB-ATC (Fig. 1 *g*), suggesting a robust downstream cellular response to TB-ATC stimulations.

Compared with SB-ATC, TB-ATC was significantly more efficient at displacing cell-bound RGD microbubbles. Application of TB-ATC for 10 s (0.015 MPa, duration of each pulse 50 ms and PRF 1 Hz) generated a larger accumulative bubble displacement (17.28 ± 3.17 μm, $n = 9$) than SB-ATC (3.92 ± 0.82; $n = 12$) using the same ultrasound parameters except for a higher acoustic pressure (0.05 MPa). As shown in Fig. 1, *i* and *j*, TB-ATC generated a much greater accumulative displacement of bubbles per unit acoustic pressure and contractile force change per unit acoustic pressure (1152.1 ± 211.4 μm MPa^{-1} and 2548.1 ± 436.7% MPa^{-1}, respectively; $n = 9$) than SB-ATC (78.4 ± 16.4 μm MPa^{-1} and 992.6 ± 124.0% MPa^{-1}, respectively; $n = 12$).

In addition to examining ATC-induced displacements of RGD microbubbles attached to NIH 3T3 fibroblasts, we also conducted experiments using microbubbles decorated with AcLDL (AcLDL microbubbles), a ligand for transmembrane metabolic receptors that cannot bind integrin receptors to elicit adhesion-mediated signaling (32). Not surprisingly, AcLDL microbubbles, without a mechanical linkage to the intracellular actin CSK, did not display the same kinetics of bubble displacements and recovery as the RGD bubbles in either the SB-ATC (Fig. 2, *a* and *b*; Movie S3) or TB-ATC (Fig. 2, *c* and *d*; Movie S4) application.

TB-ATC induced cellular responses via displacements of integrin-anchored microbubbles

We sought to ascertain the mechanism(s) of force application by TB-ATC that induced cellular responses. To compare the ATC-induced cellular responses in NIH 3T3 fibroblasts using RGD microbubbles, we also conducted experiments with NIH 3T3 fibroblasts using AcLDL microbubbles. We tracked the size and location of all cell-bound microbubbles during ATC application and measured changes in cellular CSK contractile forces using PDMS micropost arrays.

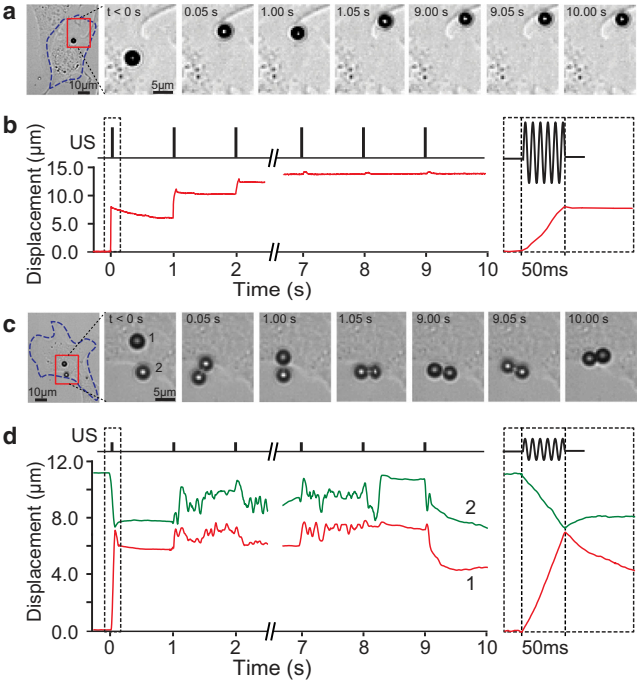

FIGURE 2 Displacements of AcLDL microbubbles attached to an NIH 3T3 fibroblast during SB-ATC and TB-ATC. (*a*) Selected images at different time points, showing a single AcLDL microbubble subjected to ultrasound pulses in SB-ATC. (*b*) Temporal evolution of the lateral displacement of the bubble in panel *a*. Inset: zoomed-in plot of the displacement during the first ultrasound pulse with a duration of 50 ms. (*c*) Selected images at different time points, showing a pair of AcLDL microbubbles during application of TB-ATC. (*d*) Temporal plots of the paired displacements of the two bubbles in panel *c* during TB-ATC. Inset: zoomed-in plot of the paired displacements during the first ultrasound pulse of 50 ms duration. Ultrasound parameters for *a* and *b*: center frequency 1.25 MHz, acoustic pressure 0.05 MPa, duration of each pulse 50 ms, and PRF 1 Hz. Ultrasound parameters for *c* and *d*: center frequency 1.25 MHz, acoustic pressure 0.015 MPa, pulse duration 50 ms, and PRF 1 Hz. To see this figure in color, go online.

Application of TB-ATC significantly increased cellular CSK contractile forces for NIH 3T3 fibroblasts with integrin-bound RGD microbubbles, and the CSK contractile force increases were positively correlated with accumulative displacements of the microbubbles (*red solid triangles* in Fig. 3 *a*; slope of linear fit ~2.0% μm^{-1}). On the other hand, NIH 3T3 fibroblasts with AcLDL microbubbles exhibited minimal changes in CSK contractile forces independently of bubble displacements (*red open triangles* in Fig. 3 *a*; slope of linear fit ~−0.1% μm^{-1}). Not surprisingly, AcLDL microbubbles showed greater movements (Fig. 3, *a* and *b*) that were more erratic, without the characteristics as RGD microbubbles (Fig. 2, *c* and *d*; Movie S4). These results suggest that displacement of the bubble-integrin-CSK linkage was critical for CSK contractile force responses in TB-ATC-treated NIH 3T3 fibroblasts.

The intercept of the linear fit of the CSK contractile force increase versus the accumulative displacement of AcLDL microbubbles (4.2%, *red open triangles* in Fig. 3 *a*) was

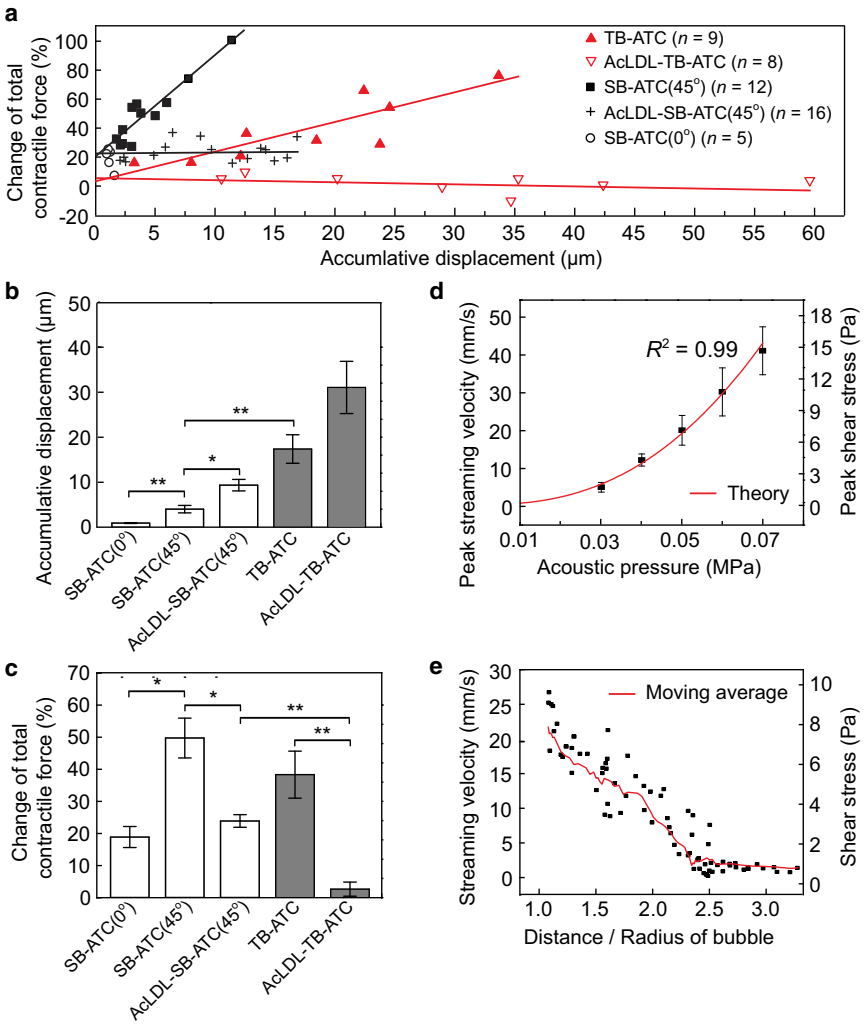

FIGURE 3 Quantification of the ATC-generated total CSK contractile force change. (*a*) Change of total CSK contractile force versus accumulative bubble displacements for different experimental groups. Solid lines represent linear fits of experimental data. (*b* and *c*) Average accumulative bubble displacements (*b*) and corresponding changes in total CSK contractile force (*c*). Ultrasound parameters: frequency 1.25 MHz, acoustic pressure 0.05 MPa for SB-ATC and 0.015 MPa for TB-ATC, PRF 1 Hz, pulse duration 50 ms. (*d*) Peak velocity of microstreaming and shear stress generated by a cavitating microbubble versus acoustic pressure. The solid line represents the theoretical calculation. (*e*) Streaming velocity and shear stress around a cavitating bubble (radius 1.8 μm) versus the distance/bubble radius. Ultrasound parameters for *d* and *e*: frequency 1.25 MHz, acoustic pressure 0.05 MPa, PRF 1 Hz, and pulse duration 50 ms. To see this figure in color, go online.

comparable to that of the RGD microbubbles (5.7%, *red solid triangles* in Fig. 3 *a*). Since the intercept represents the CSK contractile force increase that was not due to the displacement of the bubble-integrin-CSK linkage, comparable intercepts for AcLDL and RGD microbubbles implied that other aspects of ultrasound excitation of these microbubbles, such as cavitation, might elicit a response of CSK contractile force without bubble-integrin-CSK displacements.

When we compared data from NIH 3T3 fibroblasts subjected to TB-ATC or SB-ATC (incident angle 45°) that used ultrasound pulses (1.25 MHz, 50 ms pulse duration, 1 Hz PRF, and total application 10 s) at different acoustic pressures, we observed that for cells with RGD microbubbles, sustained increases of CSK contractile forces were generated by SB-ATC using acoustic pressure of 0.05 MPa, and were correlated with bubble displacements (*black solid squares* in Fig. 3 *a*) with a linear fit slope of 7.0% μm^{-1}. This slope was greater than that obtained with TB-ATC (2.0% μm^{-1}) using a lower acoustic pressure of 0.015 MPa, indicating the contribution of effects due to the higher acoustic pressure. Consistently, the intercept of the linear fit for the SB-ATC data (22%, 0.05 MPa) was also much larger than that for TB-ATC (4.2%, 0.015 MPa). SB-ATC with the same ultrasound parameters but applied at a 0° incident angle, which minimized lateral displacements of integrin-bound RGD microbubbles, generated increases of CSK contractile forces (~20%) comparable to the intercept of the linear fit for SB-ATC at a 45° incident angle (*black circles* in Fig. 3 *a*).

Compared with SB-ATC application using RGD microbubbles, SB-ATC using AcLDL microbubbles generated a much smaller increase of CSK contractile force with the same ultrasound parameters. CSK contractile force increases for SB-ATC with AcLDL microbubbles were independent of microbubble displacements (*black crosses* in Fig. 3 *a*). However, the intercept of the linear fit for SB-ATC using AcLDL microbubbles (23.1%) was greater than that for TB-ATC using AcLDL microbubbles and a lower acoustic pressure of 0.015 MPa (5.7%), and

comparable to that for SB-ATC using RGD microbubbles with the same acoustic pressure of 0.05 MPa (22%).

These results indicate that bubble cavitation, which is stronger at higher acoustic pressures (19,21,28), could induce CSK contractile force responses without bubble-FA-CSK displacements.

Effects of microbubble cavitation in ATC

We further investigated the dependence of cavitation on acoustic pressure. As microbubble cavitation generates fluid microstreaming, resulting in shear stress on nearby cells or objects (17,19–21), we measured the fluid streaming velocity induced by a cavitating microbubble attached to a cell using μPIV (Movie S5). We used ultrasound pulses with the same parameters shown in Fig. 3 with a 0° ultrasound incident angle to minimize lateral movement of bubbles. The measured streaming velocities were in an excellent agreement with theoretical predictions for a bubble undergoing stable cavitation near a flat surface (21), with increasing streaming velocities and higher shear stress at higher acoustic pressures (Fig. 3 *d*).

The shear stress generated by a cavitating bubble driven by ultrasound pulses at 0.015 MPa (as in the TB-ATC experiments shown in Fig. 3 *a*) was 0.2 Pa, much lower than the 7.1 Pa generated by an acoustic pressure of 0.05 MPa (as in the SB-ATC experiments shown in Fig. 3 *a*), which may explain the greater CSK contractile force responses and the larger intercepts of the contractile force increase versus bubble displacements observed in the SB-ATC experiments using either RGD or AcLDL microbubbles.

Cavitation-induced fluid shear stress was localized around the bubble within 3–5 μm, as streaming velocity decreased sharply with increasing distance from the bubble (Fig. 3 *e*), unlike the globally applied fluid shear stresses used in conventional methods (33,34).

Tuning ultrasound parameters for ATC operation

Based on theoretical results for ultrasound interaction with microbubbles, we performed calculations to analyze the interplay of ultrasound parameters in determining sARF, pARF, and cavitation-induced fluid streaming (Fig. 4), the main factors that determine force application by ATC.

First, we examined the effect of ultrasound frequency. For microbubbles with a radius of 1.8 μm, cavitation-induced streaming was much greater at lower frequencies (1.25 MHz in Fig. 4 *a* versus 10 MHz in Fig. 4 *b*), likely due to its relative closeness to the bubble's resonant frequency (~4 MHz for 1.8 μm radius; Fig. 4 *c*) (19,28). Resonant phenomena were evident for both pARF and sARF (Fig. 4 d). Near the resonant frequency of 1.8 μm microbubbles (~4 MHz), pARF dominated over sARF between two bubbles that were 10 μm apart. However, at higher frequencies (> 8 MHz), sARF became larger than pARF, especially at higher acoustic pressures (e.g., 0.05 MPa; Fig. 4, *d* and *f*).

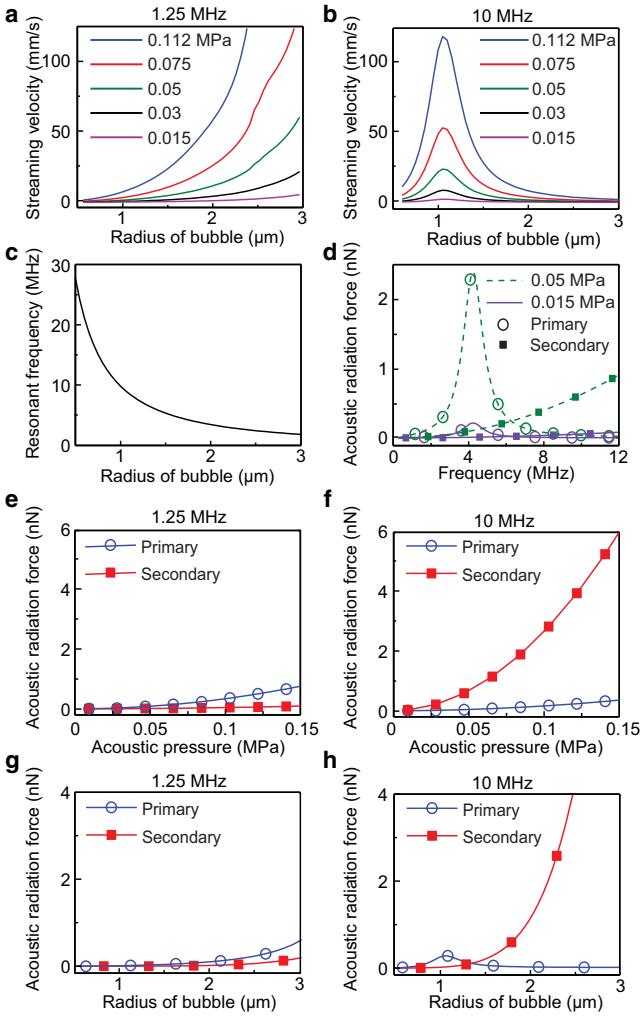

FIGURE 4 Theoretical results of ultrasound-driven microbubble responses. (*a* and *b*) Microstreaming velocity versus microbubble radius and acoustic pressure with ultrasound frequency of 1.25 MHz (*a*) or 10 MHz (*b*). (*c*) Resonant frequency of a microbubble versus bubble radius. (*d*) pARF and sARF versus ultrasound frequency with acoustic pressure of 0.05 MPa or 0.015 MPa. Bubble radius $R_0 = 1.8$ μm, distance between two bubbles $d = 10$ μm. (*e* and *f*) pARF and sARF at 1.25 MHz (*e*) and 10 MHz (*f*) versus acoustic pressure; $R_0 = 1.8$ μm and $d = 10$ μm. (*g* and *h*) pARF and sARF at 1.25 MHz (g) and 10 MHz (h) versus microbubble radius at 0.05 MPa, $d = 10$ μm, and $R_0 = 1.8$ μm. To see this figure in color, go online.

Next, we analyzed how pARF and sARF were regulated by acoustic pressure and bubble size. For two 1.8 μm bubbles 10 μm apart, sARF was comparable or greater than pARF (Fig. 4, *e* and *f*), and the difference was greater at high frequencies (e.g., 10 MHz) than at low frequencies (e.g., 1.25 MHz). At 0.05 MPa, ultrasound pulses at 1.25 MHz generated comparable sARF and pARF (Fig. 4 *g*); however, 10 MHz ultrasound generated much greater sARF than pARF (Fig. 4 *h*).

These results indicate that TB-ATC using ultrasound pulses at higher frequencies was more efficient at displacing microbubbles than SB-ATC, and the use of lower acoustic

pressures could minimize cavitation effects, consistent with our experimental results (Figs. 1 and 3).

Using ATC to assess cellular responses to mechanical stimulation

To validate the interplay of ultrasound parameters in force application in ATC and exploit the dose-dependent cellular contractile force responses (14), we implemented a dual-mode ATC protocol for both cellular probing (with minimal reactive cellular changes) and stimulation (with reactive changes). The dual-mode SB-ATC protocol (Fig. 5 *a*) consisted of a single-pulse ATC (acoustic pressure 0.025 MPa, duration 0.5 s) for rheological assessment without causing adaptive cellular changes, a multipulse ATC regime (0.05 MPa, each pulse 50 ms, PRF 1 Hz, and total duration 10 s) for cellular mechanical stimulation, and another single-pulse ATC (acoustic pressure 0.025 MPa, duration 0.5 s) 30 min afterward for poststimulation assessment. A lower acoustic pressure was chosen for the probing ultrasound pulse to minimize reactive cellular responses (Fig. 4). Control experiments were performed without ATC stimulation (*top plots* in Fig. 5 *a*).

We tracked the radius and displacement of integrin-anchored RGD microbubbles during the three stages of dual-mode SB-ATC application (Fig. 5 *a*). For the control groups of NIH 3T3 fibroblasts and hMSCs, microbubbles remained stable in size, whereas an apparent decrease in bubble radius was observed in the experimental groups with ATC stimulation (Figs. 5 *b* and 6 *a*), suggesting that microbubble cavitation subjected to the higher pressure used for ATC stimulation period compromised the protective lipid layer of the microbubbles (23). ATC probing at $t = 0$ and 30 min revealed that microbubble displacement and cell compliance, defined as bubble displacement divided by the force acting on the bubble (i.e., pARF), remained unchanged for the control groups of NIH 3T3 fibroblasts and hMSCs (Fig. 5, *c* and *d*), indicating that the ATC probing itself did not elicit cellular responsive changes.

For the experimental groups of NIH 3T3 fibroblasts and hMSCs subjected to ATC stimulation, but with the same ultrasound parameters and comparable increases of CSK contractile force (149.3% ± 3.8%, $n = 31$ for NIH 3T3 fibroblasts; 149.3% ± 3.8%, $n = 8$ for hMSCs), the RGD microbubbles bound to NIH 3T3 fibroblasts exhibited greater displacements during prestimulation ATC probing than the RGD microbubbles attached to hMSCs (Fig. 5 *c*), suggesting a higher cell compliance for NIH 3T3 fibroblasts than for hMSCs. Consistently, greater accumulative bubble displacements were also generated during ATC stimulation for NIH 3T3 fibroblasts (3.63 ± 1.2 μm, $n = 31$) than for hMSCs (1.64 ± 0.34 μm, $n = 8$). Poststimulation ATC probing revealed decreased bubble displacements for both cell types compared with prestimulation ATC probing (Fig. 5 *c*). Cell compliances also showed a reduction for both NIH 3T3 fibroblasts and hMSCs after stimulation (Fig. 5 *d*), suggesting cell stiffening due to ATC stimulation, consistent with our observation of increased cellular CSK contractile force measured using micropost sensors (Figs. 1, *g–j*, and 3 *a*) and previous results for cellular stiffening after mechanical stimulation (12,35–37).

Dual-mode TB-ATC for biomechanical assessment and stimulation

Although dual-mode SB-ATC demonstrated that tuning of acoustic pressure could control force application to cells, cavitation generated bubble shrinkage (Figs. 5 *b* and 6 *a*) at higher acoustic pressure. In addition to limiting the time window available for continual application of ATC using the same bubbles, this decrease in bubble size reduced pARF and complicated analysis of forces.

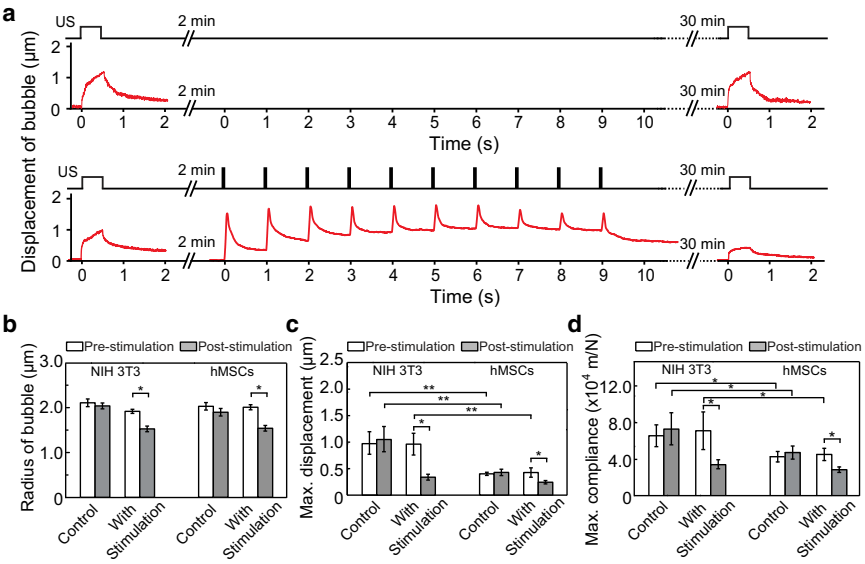

FIGURE 5 Dual-mode SB-ATC for cellular probing and stimulation. (*a*) Dual-mode SB-ATC protocol and representative bubble displacement. Top plots are for the control protocol without simulation. (*b* and *c*) Radius (*b*) and maximum displacements (*c*) of microbubbles before and after ATC stimulation for both NIH 3T3 ($n = 17$) and hMSCs ($n = 33$), and corresponding control groups of NIH 3T3 ($n = 14$) and hMSCs ($n = 12$). (*d*) Maximum cell compliance (displacement / pARF) for the experimental and control groups in *b*. Error bars represent mean ± SE. $^*p < 0.05$, $^{**}p < 0.01$, Student's *t*-test. Ultrasound parameters: center frequency 1.25 MHz, acoustic pressure 0.025 MPa and pulse duration 0.5 s for pre- and poststimulation probing; acoustic pressure 0.05 MPa and pulse duration 50 ms, PRF 1 Hz, total duration 10 s for stimulation. To see this figure in color, go online.

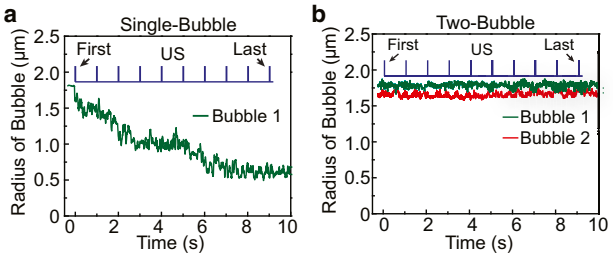

FIGURE 6 Change of bubble radius induced by SB-ATC and TB-ATC application. (*a*) Representative plot of microbubble radius as a function of time during the 10 s SB-ATC application. Ultrasound parameters: center frequency 1.25 MHz, acoustic pressure 0.05 MPa, duration of each pulse 50 ms, and PRF 1 Hz. (*b*) Representative plots of the radius of the two microbubbles during 10 s TB-ATC application. Ultrasound parameters: center frequency 10 MHz, acoustic pressure 0.12 MPa, pulse duration 10 ms, and PRF 1 Hz. To see this figure in color, go online.

As TB-ATC was efficient at displacing bubbles (Fig. 1, *i* and *j*), enabling the use of low acoustic pressures to minimize microbubble cavitation and shrinkage (Figs. 4, *a* and *b*, and 6 *b*), we implemented a dual-mode TB-ATC protocol using ultrasound pulses with a center frequency of 10 MHz to generate greater sARF than pARF (Fig. 4, *d–h*). Specifically, our dual-mode TB-ATC included a single-pulse TB-ATC (0.5 s, 0.07 MPa) for initial probing, then a multi-pulse TB-ATC for stimulation (duration of each pulse 10 ms and PRF 1 Hz or 10 Hz), and finally another single-pulse TB-ATC applied 30 min afterward for in situ assessment of cellular responses (Figs. 7 *a* and 8 *a*). We tested the dual-mode TB-ATC using hMSCs with RGD microbubbles, and tracked the microbubbles during the entire experimental process.

As expected, paired RGD microbubbles during TB-ATC application were displaced in a correlated manner without a change in amplitude during the 10 s TB-ATC stimulation (Figs. 7 *a* and 8 *a*), indicating the absence of acute reactive cellular behaviors. The bubbles were stable in size in both the control and stimulation groups (Figs. 7 *b* and 8 *b*), confirming minimal cavitation effects.

For hMSCs in the control group, a difference in maximal displacement between the two RGD microbubbles anchored at different cellular locations was detected at $t = 0$ s and 32 min (Figs. 7 *c* and 8 *c*), indicating a subcellular mechanical difference that remained unchanged without stimulation. For the hMSCs subjected to TB-ATC stimulations, RGD microbubbles at different subcellular locations exhibited different displacements at $t = 0$ before stimulation (Figs. 7 *c* and 8 *c*). Interestingly, this difference was reduced 30 min after TB-ATC stimulation at a PRF of 1 Hz (Fig. 7 *c*) and even more so at a PRF of 10 Hz (Fig. 8 *c*), for which more pulses were delivered within the 10 s duration, suggesting a dose-dependent CSK redistribution and homogenization by TB-ATC stimulation. In addition, whereas the bubble with a greater initial maximum displacement (bubble 1) exhibited a significant decrease in displacement 30 min after TB-ATC stimulation (Figs. 7 *c* and 8 *c*), the other bubble (bubble 2) sustained a small (1 Hz PRF stimulation; Fig. 7 *c*) or significant (10 Hz PRF stimulation; Fig. 8 *c*) decrease, suggesting dose-dependent cellular stiffening.

DISCUSSION

In previous studies, acoustic radiation forces were exploited primarily to spatially trap a single particle (38) or a collection of particles (39), and to target microbubbles in molecular ultrasound imaging (40). In contrast, SB-ATC and TB-ATC use acoustic radiation forces to displace integrin-bound microbubbles on cell surfaces to generate subcellular strains and stresses through a bubble-integrin-CSK connection. In particular, TB-ATC uses the acoustic interaction force between two bubbles (sARF) to displace paired integrin-bound microbubbles in a correlated manner and generate

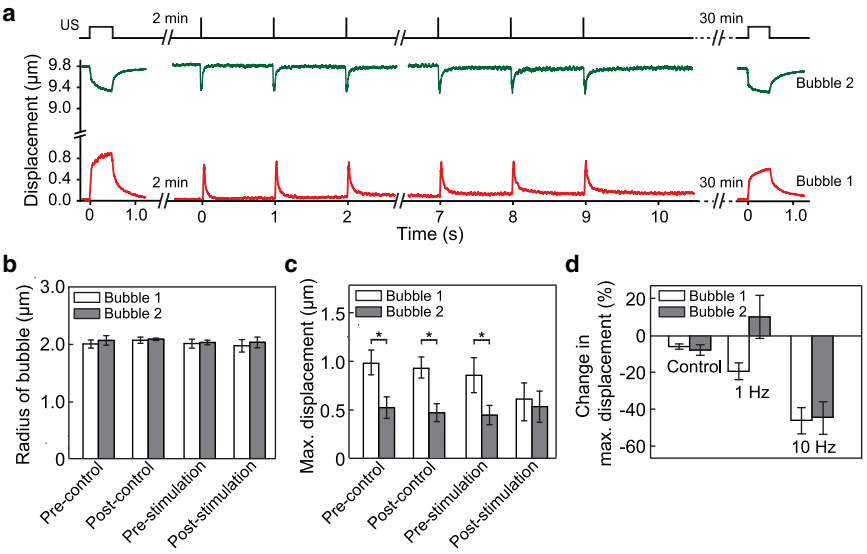

FIGURE 7 Dual-mode TB-ATC probing and stimulation of hMSCs. (*a*) Schematic of dual-mode TB-ATC and representative microbubble displacements. (*b* and *c*) Radius (*b*) and maximum displacements (*c*) of the paired microbubbles before and after TB-ATC stimulation for experimental ($n = 12$) and control ($n = 14$) groups. Error bars represent mean ± SE. $^*p < 0.05$, Student's *t*-test. Ultrasound parameters for *a–c*: center frequency 10 MHz, acoustic pressure 0.07 MPa and pulse duration 0.5 s for pre- and poststimulation probing, acoustic pressure 0.12 MPa, pulse duration 10 ms, PRF 1 Hz, total duration 10 s for stimulation. (*d*) Change of maximum displacement for each of bubbles subjected to TB-ATC stimulation with PRF of 1 or 10 Hz. To see this figure in color, go online.

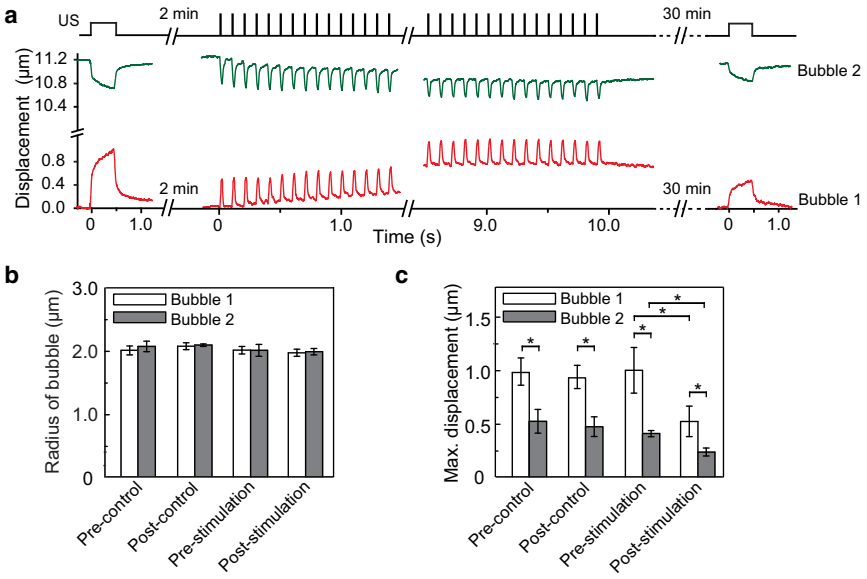

FIGURE 8 Dual-mode TB-ATC for cellular probing and stimulation. (*a*) Schematic of a combined ultrasound protocol including single-pulse TB-ATC and multipulse TB-ATC, and representative plots of the displacements of microbubbles throughout the three stages of TB-ATC application. (*b*) Microbubble radius for the bubble in the paired microbubbles before and after TB-ATC stimulation for the experimental ($n = 16$) and control ($n = 14$) groups. (*c*) Maximal displacements of microbubbles in the experimental and control groups in panel *b*. Error bars are mean ± SE. $*p < 0.05$, Student's *t*-test. Ultrasound parameters: center frequency 10 MHz, acoustic pressure 0.07 MPa and pulse duration 0.5 s for pre- and poststimulation TB-ATC probing; acoustic pressure 0.12 MPa, pulse duration 10 ms, PRF 10 Hz, total application duration 10 s for TB-ATC stimulation. To see this figure in color, go online.

spatiotemporally controlled forces on live cells. This unique mechanism enables simple yet efficient force application, quantitative analysis, and convenient experimental implementation. For example, since sARF drives the microbubbles directly toward each other, TB-ATC requires no specific alignment of the direction of the incident ultrasound pulses, which can be time-consuming and cause errors leading to inconsistent results. The kinetics and size of the bubbles can be easily monitored for quantification. Since the same-amplitude sARF acted on each microbubble in a pair, we could conveniently use the difference in their displacements to make rapid in situ assessments of the subcellular differences in cell mechanical properties without the absolute values of the actual forces acting on the bubbles.

Since sARF increases as the bubbles move closer to each other, conventional rheological analysis cannot be directly applied to calculate cell compliance (i.e., displacement/force) without appropriate modification. However, sARF can be determined by the separation distance between the two bubbles, which can be precisely measured experimentally. Thus, with the known force and its response, one can obtain quantitative information regarding the mechanical properties of the cells in the location of the bubbles. In this study, we obtained the acoustic radiation forces from the measured acoustic pressures using validated theoretical expressions; however, in future studies we plan to directly determine these forces to characterize their dependence as a function of various relevant acoustic parameters.

Lipid-encapsulated microbubbles have been used clinically as an ultrasound imaging contrast agent (16). Thus, microbubble-facilitated ATC may provide a biocompatible strategy for mechanical probing and manipulation of cellular functions even in vivo. Functionalization of microbubbles can be easily achieved to permit targeting of specific cell-surface receptors (41) and explore their roles in cell mechanotransduction. Cell-bound microbubbles exhibit no internalization and can be easily eliminated without leaving behind exogenous materials, which is desirable for continual use and longitudinal studies of the treated cells for further investigations and translational applications. Microbubbles may also be reapplied as needed. The robust ultrasound interaction with microbubbles allows the generation of a wide range and different forms of mechanical forces to cells. A rich variety of ultrasound protocols tailored to specific applications can be readily implemented using simple systems. Broadly applied or focused ultrasound beams can be used to stimulate either a large ensemble of single cells simultaneously or a small group of single cells with subcellular resolution via the attached microbubbles on cell surfaces.

CONCLUSIONS

TB-ATC generates subcellular strains and stresses by displacing paired integrin-bound microbubbles on cell surfaces using sARF. Tuning of ultrasound parameters allows controlled force application for biomechanical probing and stimulation of cells in an integrated platform, providing an advantageous tool for cell mechanics and mechanobiology studies.

SUPPORTING MATERIAL

Five movies are available at http://www.biophysj.org/biophysj/supplemental/S0006-3495(14)01257-0.

ACKNOWLEDGMENTS

This work was supported by the National Science Foundation (CMMI 1129611 and CBET 1149401 to J.F.), the National Institutes of Health

(R21HL114011 to J.F., R01CA116592 to C.X.D., and R21EB017078 to C.X.D. and J.F.), and the American Heart Association (12SDG12180025 to J.F.). The Lurie Nanofabrication Facility at the University of Michigan, a member of the National Nanotechnology Infrastructure Network funded by the National Science Foundation, supported the microfabrication.

REFERENCES

1. Wozniak, M. A., and C. S. Chen. 2009. Mechanotransduction in development: a growing role for contractility. *Nat. Rev. Mol. Cell Biol.* 10:34–43.
2. Hahn, C., and M. A. Schwartz. 2009. Mechanotransduction in vascular physiology and atherogenesis. *Nat. Rev. Mol. Cell Biol.* 10:53–62.
3. Discher, D. E., P. Janmey, and Y. L. Wang. 2005. Tissue cells feel and respond to the stiffness of their substrate. *Science.* 310:1139–1143.
4. Hoffman, B. D., C. Grashoff, and M. A. Schwartz. 2011. Dynamic molecular processes mediate cellular mechanotransduction. *Nature.* 475:316–323.
5. Geiger, B., J. P. Spatz, and A. D. Bershadsky. 2009. Environmental sensing through focal adhesions. *Nat. Rev. Mol. Cell Biol.* 10:21–33.
6. Chen, C. S. 2008. Mechanotransduction—a field pulling together? *J. Cell Sci.* 121:3285–3292.
7. Vogel, V., and M. Sheetz. 2006. Local force and geometry sensing regulate cell functions. *Nat. Rev. Mol. Cell Biol.* 7:265–275.
8. Rowat, A. C. 2009. Physical properties of the nucleus studied by micropipette aspiration. *Methods Mol. Biol.* 464:3–12.
9. Svoboda, K., C. F. Schmidt, …, S. M. Block. 1993. Direct observation of kinesin stepping by optical trapping interferometry. *Nature.* 365:721–727.
10. Mackay, J. L., and S. Kumar. 2013. Measuring the elastic properties of living cells with atomic force microscopy indentation. *Methods Mol. Biol.* 931:313–329.
11. Chen, J., B. Fabry, …, N. Wang. 2001. Twisting integrin receptors increases endothelin-1 gene expression in endothelial cells. *Am. J. Physiol. Cell Physiol.* 280:C1475–C1484.
12. Chowdhury, F., S. Na, …, N. Wang. 2010. Material properties of the cell dictate stress-induced spreading and differentiation in embryonic stem cells. *Nat. Mater.* 9:82–88.
13. Wang, N., J. P. Butler, and D. E. Ingber. 1993. Mechanotransduction across the cell surface and through the cytoskeleton. *Science.* 260:1124–1127.
14. Fan, Z., Y. Sun, …, J. Fu. 2013. Acoustic tweezing cytometry for live-cell subcellular modulation of intracellular cytoskeleton contractility. *Sci. Rep.* 3:2176.
15. Goldberg, B. B., J.-B. Liu, and F. Forsberg. 1994. Ultrasound contrast agents: a review. *Ultrasound Med. Biol.* 20:319–333.
16. Kaul, S. 2008. Myocardial contrast echocardiography: a 25-year retrospective. *Circulation.* 118:291–308.
17. O'Brien, Jr., W. D. 2007. Ultrasound-biophysics mechanisms. *Prog. Biophys. Mol. Biol.* 93:212–255.
18. Deng, C. X., and F. L. Lizzi. 2002. A review of physical phenomena associated with ultrasonic contrast agents and illustrative clinical applications. *Ultrasound Med. Biol.* 28:277–286.
19. Wu, J. 2007. Shear stress in cells generated by ultrasound. *Prog. Biophys. Mol. Biol.* 93:363–373.
20. Xie, Y., C. Zhao, …, T. J. Huang. 2013. Optoacoustic tweezers: a programmable, localized cell concentrator based on opto-thermally generated, acoustically activated, surface bubbles. *Lab Chip.* 13:1772–1779.
21. Marmottant, P., and S. Hilgenfeldt. 2003. Controlled vesicle deformation and lysis by single oscillating bubbles. *Nature.* 423:153–156.
22. Prentice, P., A. Cuschieri, …, P. Campbell. 2005. Membrane disruption by optically controlled microbubble cavitation. *Nat. Phys.* 1:107.
23. Fan, Z., H. Liu, …, C. X. Deng. 2012. Spatiotemporally controlled single cell sonoporation. *Proc. Natl. Acad. Sci. USA.* 109:16486–16491.
24. Dayton, P. A., K. E. Morgan, …, K. W. Ferrara. 1997. A preliminary evaluation of the effects of primary and secondary radiation forces on acoustic contrast agents. *IEEE Trans. Ultrason. Ferroelectr. Freq. Control.* 44:1264–1277.
25. Zhou, Y., K. Yang, …, C. X. Deng. 2012. Controlled permeation of cell membrane by single bubble acoustic cavitation. *J. Control. Release.* 157:103–111.
26. Fan, Z., D. Chen, and C. X. Deng. 2013. Improving ultrasound gene transfection efficiency by controlling ultrasound excitation of microbubbles. *J. Control. Release.* 170:401–413.
27. Erpelding, T. N., K. W. Hollman, and M. O'Donnell. 2007. Bubble-based acoustic radiation force using chirp insonation to reduce standing wave effects. *Ultrasound Med. Biol.* 33:263–269.
28. Marmottant, P., and S. Hilgenfeldt. 2004. A bubble-driven microfluidic transport element for bioengineering. *Proc. Natl. Acad. Sci. USA.* 101:9523–9527.
29. Goertz, D. E., N. de Jong, and A. F. W. van der Steen. 2007. Attenuation and size distribution measurements of Definity and manipulated Definity populations. *Ultrasound Med. Biol.* 33:1376–1388.
30. Yang, M. T., J. Fu, …, C. S. Chen. 2011. Assaying stem cell mechanobiology on microfabricated elastomeric substrates with geometrically modulated rigidity. *Nat. Protoc.* 6:187–213.
31. Fu, J., Y. K. Wang, …, C. S. Chen. 2010. Mechanical regulation of cell function with geometrically modulated elastomeric substrates. *Nat. Methods.* 7:733–736.
32. Meyer, C. J., F. J. Alenghat, …, D. E. Ingber. 2000. Mechanical control of cyclic AMP signalling and gene transcription through integrins. *Nat. Cell Biol.* 2:666–668.
33. Mann, J. M., R. H. Lam, …, J. Fu. 2012. A silicone-based stretchable micropost array membrane for monitoring live-cell subcellular cytoskeletal response. *Lab Chip.* 12:731–740.
34. Lam, R. H. W., Y. Sun, …, J. Fu. 2012. Elastomeric microposts integrated into microfluidics for flow-mediated endothelial mechanotransduction analysis. *Lab Chip.* 12:1865–1873.
35. Deng, L., N. J. Fairbank, …, G. N. Maksym. 2004. Localized mechanical stress induces time-dependent actin cytoskeletal remodeling and stiffening in cultured airway smooth muscle cells. *Am. J. Physiol. Cell Physiol.* 287:C440–C448.
36. Matthews, B. D., D. R. Overby, …, D. E. Ingber. 2006. Cellular adaptation to mechanical stress: role of integrins, Rho, cytoskeletal tension and mechanosensitive ion channels. *J. Cell Sci.* 119:508–518.
37. Icard-Arcizet, D., O. Cardoso, …, S. Hénon. 2008. Cell stiffening in response to external stress is correlated to actin recruitment. *Biophys. J.* 94:2906–2913.
38. Lee, J., K. Ha, and K. K. Shung. 2005. A theoretical study of the feasibility of acoustical tweezers: ray acoustics approach. *J. Acoust. Soc. Am.* 117:3273–3280.
39. Ding, X., S. C. Lin, …, T. J. Huang. 2012. On-chip manipulation of single microparticles, cells, and organisms using surface acoustic waves. *Proc. Natl. Acad. Sci. USA.* 109:11105–11109.
40. Borden, M. A., J. E. Streeter, …, P. A. Dayton. 2013. In vivo demonstration of cancer molecular imaging with ultrasound radiation force and buried-ligand microbubbles. *Mol. Imaging.* 12:357–363.
41. Unnikrishnan, S., and A. L. Klibanov. 2012. Microbubbles as ultrasound contrast agents for molecular imaging: preparation and application. *AJR Am. J. Roentgenol.* 199:292–299.
42. Faez, T., D. Goertz, and N. De Jong. 2011. Characterization of Definity™ ultrasound contrast agent at frequency range of 5-15 MHz. *Ultrasound Med. Biol.* 37:338–342.
43. Park, J., Z. Fan, and C. X. Deng. 2011. Effects of shear stress cultivation on cell membrane disruption and intracellular calcium concentration in sonoporation of endothelial cells. *J. Biomech.* 44:164–169.